

Exploring the effects of carbon meso-structure and macrostructure on the rate performance of porous carbon supercapacitors

Jocelyn E. Zuliani¹ · Charles Q. Jia¹ · Donald W. Kirk¹

Received: 14 June 2017 / Accepted: 25 September 2017 / Published online: 4 October 2017
© Springer Science+Business Media B.V. 2017

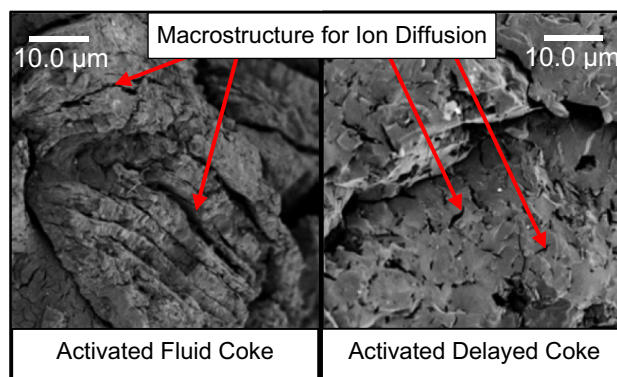
Abstract Electrochemical double-layer capacitors are promising energy storage devices with high power density, moderate energy density, rapid charging rates, and high cycle life. In order to maximize energy density, highly porous carbon materials are often incorporated in the electrodes. The structure of the porous carbon network is critical to ensure high power delivery and charging rate. In this study, two types of oil sands petroleum cokes, from either batch or continuous industrial coking, were used to prepare porous carbon samples. The two activated petroleum coke samples have similar chemical compositions, specific surface areas, and pore size distributions, but due to the different industrial coking methods, the two samples have differing macrostructures and porous networks. Using mercury intrusion porosimetry and scanning electron microscopy, the meso-structure, macrostructure, and pore connectivity of the two samples were characterized and compared to the capacitance performance of the activated coke samples. The results show that, in order to ensure high rate performance, especially in ion depleted electrolyte scenarios, the porous carbon samples must have an interconnected network of pores between 10 and 1000 nm in diameter. These pore sizes are shown to improve the rate of ion diffusion, and allow greater capacitance values to be achieved at rapid charging rates.

Electronic supplementary material The online version of this article (doi:10.1007/s10800-017-1123-9) contains supplementary material, which is available to authorized users.

✉ Donald W. Kirk
don.kirk@utoronto.ca

¹ Department of Chemical Engineering & Applied Chemistry, University of Toronto, 200 College St., Toronto, ON M5S 3E5, Canada

Graphical abstract



Keywords Electrical energy storage · Supercapacitors · Ion diffusion · Porous carbon · Charging rate

1 Introduction

Electrical energy storage is critical for many applications from portable electronics, to electric vehicles, and grid power management and supply. There is a broad array of energy storage devices offering different power and energy properties. Supercapacitors are one type of energy storage device, which offer higher power density than that of traditional batteries and fuel cells, and a moderate energy density, as well as high cycle life, and rapid charging times [1–4]. Supercapacitors can be divided into three categories, electrochemical double-layer capacitors (EDLCs), pseudocapacitors, and hybrid capacitors. EDLCs store energy by physical charge separation and ion adsorption on the surface of a porous electrode. In contrast, pseudocapacitors store energy by highly reversible, rapid charge transfer reactions,

typically employing transition metal oxides as the active material. Finally, hybrid capacitors combine the mechanisms of both EDLCs and pseudocapacitors to enhance energy storage capacity [1–15]. This study will focus on EDLC devices and phenomena that occur in the electrical double layer (EDL).

The capacitive energy storage in EDLCs is due to the formation of an EDL on the surface of a porous carbon electrode. A charge is applied to the porous electrode, and counter-ions in the electrolyte solution migrate and adsorb on the surface of the electrode to balance the charge. This is known as the EDL [1, 2, 4, 6, 15, 16]. The energy stored in the EDL is directly proportional to the capacitance of the EDL; therefore, capacitance is often the metric used to evaluate the performance of an electrode material for an EDLC device.

The maximum achievable capacitance, or intrinsic capacitance, in a given electrolyte determines the maximum energy density of a material. This is a key performance metric that is often used to evaluate the suitability of a material for EDLC devices. The intrinsic capacitance is determined by the total accessible surface area, the pore size distribution, and the electrolyte properties, such as ion size, conductivity, and relative dielectric constant. Significant research effort has been focused on increasing the intrinsic or maximum achievable capacitance in order to increase energy density to compete with developing battery technology [7–9, 12–15, 17–20]. While there remains a debate in the research community regarding the origin of enhanced capacitance [7, 21–25], the majority of the results suggest that high microporosity (pore diameters < 2 nm) leads to increased energy density [17, 18, 25–38]. Therefore, typically porous carbon materials are prepared with high microporosity in order to enhance their maximum achievable capacitance. However, preparing porous carbon materials with extremely high microporosity, and low meso- and macroporosity limits the ability of ions to quickly diffuse into and out of the electrode material during charging/discharging [15, 39–43]. This limitation may not be an issue for microscale research electrodes often reported in literature. The rate performance of a material must be characterized in order to determine its suitability for practical EDLC devices.

The rate performance of a material is the relationship between measured capacitance and charging/discharging rate. The rate performance can also be described as capacitance retention and is presented as a percentage of the maximum measurable capacitance, which is achieved at the lowest charging rate. Ideal materials would retain a high capacitance at high charging rates, in order to maximize both energy density (high capacitance), and power density (high discharge currents). The rate performance of an EDLC device is associated with its equivalent series resistance, consisting of the electrical resistance of the electrode and

electrolyte and the resistance associated with ionic diffusion through the separator and in the porous carbon structure. The electronic resistances are fixed parameters controlled by the structure, and conductivity of the carbon material, the electrolyte conductivity, and the EDLC device configuration [1–3, 15]. However, the resistance associated with ionic diffusion may be affected by the charging rate and time. As the charging rate, either current density or sweep rate, is increased, the measurable capacitance tends to decrease due to limitations associated with ion diffusion into and out of the porous carbon electrodes. The resistance to ion diffusion is associated with the pore structure, connectivity, and size; therefore, research efforts have been made to determine the ideal pore structure to promote ion diffusion and transport. Yamada et al. [44] designed an experiment to investigate the effects of macroporous structure, using carbon beads with a starburst porous structure. This structure consisted of channels running from the edge of the particle to the center and the pore depth was assumed to be the radius of the particle. Yamada et al. concluded that the resistance associated with ion diffusion between particles and in the macrostructure of the particles had a greater effect on the performance, compared to diffusion within the particle channels. This leads to their conclusion that it is critical to control the macrostructure to ensure effective ion diffusion into and out of the pores [44].

Templating techniques can be used to control the macrostructure, increase the connectivity and mesoporosity of porous carbon, while retaining high microporosity. These carbon materials are termed hierarchical porous carbon materials, in which a smooth succession from large macropores to sub-nanometer pores is created using template materials, such as silica, zeolites, and metal carbides. Generally, increasing the mesoporosity increases the rate performance in these hierarchical porous carbon materials [15, 39–43, 45]. However, templating processes require many detailed processing steps in order to prepare porous carbon, which increases the cost and time to prepare materials [15]. It would be ideal to retain the structure of the carbon precursor, in order to promote ion diffusion and simplify preparation procedures.

In this study, activated carbon is produced from Canadian Oil Sands by-product petroleum coke. Petroleum coke is the solid carbon product that is produced when bitumen is upgraded to synthetic crude oil. There are two types of coking used in Canada, delayed coking, which is a batch process, and fluid coking, which is a continuous process. The coke produced from delayed coking is initially extracted from the coker reactor and crushed. This coke has a very large and random particle size and must be further crushed to generate a free-flowing uniform powder. However, fluid coking is a continuous coking process in which coke particles are recirculated between a heater and a coker reactor.

Due to this two-step process, the coke particles have concentric carbon layers deposited during each coking cycle. This leads to a free-flowing powder of nearly spherical particles. These two coking processes result in coke products with similar chemical composition, but different mesoscale and macroscale structures [46–50]. These differences in pore structure will be used to investigate the effect of larger pores on the rate performance of a material.

Petroleum coke has been used in previous studies as the precursor for activated carbon preparation. Initial studies resulted in a low specific surface area (SSA) material [47]; however, further optimization of the activation process has generated chemically activated petroleum coke with SSA values greater than $2000 \text{ m}^2 \text{ g}^{-1}$ [48].

The two activated petroleum coke materials, activated delayed coke (ADC) and activated fluid coke (AFC) have been prepared with similar SSAs, chemical compositions, and pore size distributions for pores $< 10 \text{ nm}$ in diameter. However, as explained above, these two materials have different meso-structures and macrostructures, which are the subject of the work to determine the effect of electrolyte ion diffusion in the electrode and the rate performance of the materials.

2 Experimental

2.1 Raw materials

Oil sands petroleum coke is produced during upgrading of bitumen to synthetic crude oil, by a process known as coking. As described above, due to the coking techniques used at different oil sands facilities, oil sands delayed coke has a random carbon macrostructure, and oil sands fluid coke has a concentric layered carbon structure.

Oil sands fluid petroleum coke was used as one of the raw materials to prepare porous carbon for the EDLC electrodes; the fluid coke was supplied by the Canadian Oil Sands Industry. The coke was prepared for activation by sieving to a particle size between 150 and 212 μm . The second type of coke used to prepare porous carbon was oil sands delayed coke, supplied by the Canadian Oil Sands Industry. Since this coke is prepared in a batch coking process, the as received particles are much larger. The particles were first ground, and then sieved to a particle size between 150 and 212 μm . After the particle size was controlled, the raw coke materials were activated using as received potassium hydroxide from Sigma Aldrich.

The electrodes were prepared using carbon black, supplied by Fisher Scientific, as a conductive additive. The carbon particles were bound together using polytetrafluoroethylene, which was supplied in 60 wt% dispersion and

used as received from Sigma Aldrich. All solvents were used as supplied.

2.2 Porous carbon preparation

Porous carbon materials were prepared using potassium hydroxide chemical activation. The activating conditions are listed in Table 1 below, and were adapted from the procedure presented in Zuliani et al. [48, 51]. Two activated petroleum coke samples were prepared, the AFC sample was prepared using oil sands fluid coke as the carbon source and the ADC sample was prepared using oil sands delayed coke as the raw material. The raw coke particles were mixed with potassium hydroxide in a mass ratio of 2.5:1 KOH:coke, and 1 mL of water per gram of coke. Methanol, 0.3 g, was added to improve the wettability of the petroleum coke. The mixtures were allowed to stand at ambient conditions for 20 h.

Activation was performed using a vertical tube furnace, with a steel crucible sample holder suspended in the middle of the furnace. Activations were performed under an inert nitrogen atmosphere to prevent coke combustion. After activation, the material was cooled under nitrogen to room temperature. The porous carbon was washed with distilled water and dilute hydrochloric acid (five-fold dilution of pure hydrochloric acid) to remove residual potassium hydroxide and potassium carbonate.

2.3 Physicochemical characterization

The goal of the following analytical techniques is to characterize the physical and chemical features of the two porous carbon samples. By using these various analytical techniques, the similarities and differences in the physical and chemical properties of the porous carbon samples can be identified. Ideally, only a single physical or chemical feature will vary between the samples, allowing for isolation

Table 1 Activating conditions to prepare AFC and ADC

	AFC	ADC
Raw material	Oil sands fluid petroleum coke	Oil sands delayed petroleum coke
Activating agent	KOH	
Mass ratio activating agent (KOH:Coke)	2.5:1	
Holding time at room temperature	20 h	
KOH melting temperature	400 °C	
KOH melting time	2 h	
Pyrolysis temperature	850 °C	
Pyrolysis time	2 h	

of its relationship with the performance of the material in an EDLC.

2.3.1 Specific surface area and pore size distribution

The SSA of the carbon materials was calculated using isothermal data from both nitrogen gas adsorption, at 77 K, and carbon dioxide gas adsorption, at 273 K. In order to calculate the SSA and pore size distributions for pores < 1 nm in diameter, non-local density functional theory was used to analyze the carbon dioxide isotherm. The SSA and pore size distribution for pores with diameters greater than 1 nm is estimated using quenched solid density functional theory, which accounts for pore roughness, in order to analyze the nitrogen gas isotherms at 77 K. The intersection point of the pore size distributions estimated from the carbon dioxide and nitrogen gas isotherms were overlaid in order to determine that the intersection point was approximately 1 nm. Jagiello et al. also demonstrated that the carbon dioxide and nitrogen gas models can be combined in order to generate a unified pore size distribution for broad pore size distribution microporous carbon materials [52]. Further details on the application of the combined adsorption models can be found in the study performed by Caguiat et al. [53].

Isothermal gas adsorption was performed using a Autosorb 1-C, supplied by Quantachrome Instruments. During this analysis process, gas (nitrogen or carbon dioxide) was injected into a sealed container at different pressures. The volume of gas adsorbed on the surface of the porous carbon samples is calculated based on the change in pressure in the vessel once it has reached equilibrium. The change in pressure is the difference between the pressure at equilibrium and the pressure initially injected into the vessel [54, 55]. The isothermal data is then used to estimate the SSA, specific pore volume, and pore size distribution of the carbon materials as outlined above [52–55]. The SSA, specific pore volume, and pore size distributions characterize the physical structure of the activated petroleum coke samples for features below 10 nm in diameter. These characteristics affect the performance of the activated carbon material in an EDLC device, primarily affecting the maximum achievable capacitance. The SSA value is also used a normalization parameter for capacitance, to calculate the SSA-normalized capacitance.

2.3.2 Mercury intrusion porosimetry

Mercury intrusion porosimetry analysis was performed on the AFC and ADC samples in order to characterize the pore size distribution and pore volume for pores between 100,000 and 3.5 nm. Prior to analysis, the samples were dried overnight in a desiccator to remove moisture.

Mercury intrusion porosimetry is a similar technique to the gas adsorption technique outlined above. In this analysis, mercury, a non-wetting fluid, is injected into a closed vessel with the porous material. The pressure is then gradually increased; as the pressure is increased, the volume of mercury intruded into the sample is measured by the instrument. At lower applied pressure, mercury intrudes into the largest pores, and as the pressure is increased, the mercury intrudes into the smaller pores. In order to determine the pore diameter, the Washburn equation is used, which relates the applied pressure to pore diameter at equilibrium. This equation calculates the minimum pore size that is penetrable at a given pressure through a force balance between pressure, surface tension of mercury, and contact angle, assuming a cylindrical pore shape. The Washburn equation is presented in Eq. 1, where D_p is the pore diameter, γ is the surface tension of mercury, θ is the contact angle of mercury on the porous sample, and P is the applied pressure [56].

$$D_p = - \frac{4\gamma \cos(\theta)}{P} \quad (1)$$

The mercury intrusion porosimetry technique is used to calculate the relationship between cumulative intrusion volume and pore diameter, which provides a characterization of the meso-structure and macrostructure of the porous carbon materials. This information provides further insight into the physical structure of the carbon samples for larger pore diameters compared to the isothermal gas adsorption.

2.3.3 Carbon density measurements

The skeletal density of a carbon sample is a measurement of the density of the carbon material itself, excluding the void spaces. This was determined using a Ultrapycnometer 1000, supplied by Quantachrome Instruments, with helium gas, in continuous flow mode. During the analysis, the carbon sample is placed in a chamber of a known volume. The chamber is sealed and evacuated, then a fixed volume of helium gas is injected into the system and the equilibrium pressure is measured. Based on the equilibrium pressure, the volume of the carbon skeleton is calculated and compared to the mass of the sample. The skeletal density of the carbon sample can be compared to known carbon structures (sp², sp³, or amorphous). This provides insight into the crystal structure of the carbon materials.

The bulk density of a porous carbon material is a measure of the density including the air in the void spaces. The bulk density of the materials was determined by measuring the mass and volume of a sample in a 10 mL graduated cylinder. To ensure the bulk density measurements were representative, and that the void space was minimized, the samples were tapped several times to allow the particles to settle.

The bulk density can be used to characterize the pore volume and void spacing of the carbon material. This information is important when calculating the capacitance of a carbon material in order to determine its capacitance per unit mass and per unit volume. The bulk density is important to consider when comparing the performance of different porous carbon samples for EDLCs, especially if the carbon materials have different pore volumes.

2.3.4 Electron microscopy imaging

Scanning electron microscopy (SEM) was performed on the samples to determine the macroscopic structures. An ultra-high resolution SEM, SU8230, supplied by Hitachi, was used with an accelerating voltage of 500 V in order to characterize and image the porous carbon particles.

SEM analysis is performed to provide a visual image of the porous carbon sample. In this analysis, the carbon sample is placed in a vacuum chamber. The sample is irradiated with electrons at a specified accelerating voltage, (500 V in this study). The electrons are reflected from the sample and data is collected by sensors in the instrument. This information is mathematically transformed into an image of the carbon surface. Due to the low molecular mass of carbon, a low accelerating voltage was selected to avoid electron penetration into the sample, and artificial smoothing of the carbon surface. The SEM analysis provided visual insight into the carbon structure and was used to understand and characterize the macrostructure of the porous carbon samples.

2.3.5 Elemental chemical analysis

Elemental analysis of the carbon, hydrogen, nitrogen, oxygen, and sulfur content of the porous carbon samples was performed using a CE 440 elemental analyzer, supplied by Exeter Analytical. Elemental content was determined by combustion of a small sample (1–2 mg) and quantification of the combustion product. The elemental chemical analysis characterizes the chemical composition of the porous carbon samples. The chemical composition of the carbon samples can affect their electrochemical performance, since surface functional groups may undergo rapid charge transfer reactions. These rapid charge transfer reactions enhance the observed capacitance. Therefore, it is important to characterize and control the chemical composition of the carbon samples.

2.3.6 X-ray photoelectron spectroscopy analysis

In order to characterize the oxygen functional groups on the surface of the activated petroleum coke samples, X-ray photoelectron spectroscopy was performed. The X-ray

photoelectron spectroscopy analysis was performed using a KAlpha⁺ X-ray photoelectron spectrometer, with an Al K_α X-ray source, supplied by Thermo Scientific.

X-ray photoelectron spectroscopy is used to characterize the functional groups on the carbon surface; this study focuses on oxygen functional groups. This analysis provides information on the bonding energy of the oxygen (i.e. bonding energy of oxygen with the carbon surface). In this analysis, the carbon surface is irradiated with X-ray photons of a known energy. These X-ray photons interact with the carbon surface, causing the electrons to be released from the surface. The kinetic energy of the electrons is measured by a detector. The measurement of the kinetic energy of the released electron allows the binding energy and hence, the functional group to be determined.

The information collected from the X-ray photoelectron spectroscopy analysis was used to characterize the oxygen functional groups on the carbon surface. Oxygen is known to undergo charge transfer reactions in an alkaline electrolyte. Therefore, it is important to quantify and control the oxygen functional groups that are electrochemically active in alkaline solutions, in order to compare the performance of porous carbon materials in EDLCs.

2.4 Electrochemical characterization

Flexible composite electrodes were prepared using 90 wt% activated petroleum coke, 6 wt% carbon black, and 4 wt% polytetrafluoroethylene. Carbon black was added to the mixture to improve electrode conductivity, while polytetrafluoroethylene polymer was used as a binder. The carbon black and activated petroleum coke were mixed with 4 mL of water and 3 mL of isopropanol. After obtaining a uniform mixture, the polytetrafluoroethylene suspension, diluted with 1 mL of water, was added to the mixture. The mixture was heated slowly to evaporate the water and generate a malleable semi-solid mixture. The mixture was then rolled into a thin film of 0.7–0.8 mm in thickness, and cut into circular electrodes with a diameter of 15.9 mm and a projected area of 198 mm². The mass of each electrode was between 45 and 50 mg.

The electrodes were dried in an oven for 4 h. The EDLC 2-electrode test cells were prepared using a nickel mesh as the current collector and polyphenylene sulfide as the porous non-conductive separator. EDLC cells were prepared using AFC electrodes and ADC electrodes. In order to ensure the electrodes and separator were fully wet by the electrolyte, the prepared cells were placed in the potassium hydroxide electrolyte, with concentrations of either 0.4 or 4 M, for 7 days.

The concentrated 4 M potassium hydroxide electrolyte was used in the EDLCs as it provides an ion rich solution where ample ions are available to match the applied surface

charge and to maximize the measured capacitance. However, in this concentrated electrolyte, the effects of ion diffusion in the carbon materials may be negligible or masked due to the large number of ions in the solution. Therefore, diluted potassium hydroxide electrolyte, 0.4 M, was used in order to make the effects of ion diffusion more prominent and depict an ion depleted scenario. This ion depleted scenario may occur in cases where electrolyte volume is a limiting factor, as well as when the EDLC is operated at high rates. While this dilute electrolyte concentration may not be realistic to use in a commercial EDLC, the usage of a low concentration electrolyte in these experiments has provided insight into the relationship between carbon electrode performance and the meso-structure and macrostructure of the carbon material.

Electrochemical analysis was performed using a Solartron 1280 B/C potentiostat, using a potential window of 0.8 V, with both constant current cycling, for current densities between 25 and 7500 mA g⁻¹, and cyclic voltammetry, for sweep rates between 1 and 100 mV s⁻¹. Normalized values are reported to the mass of activated petroleum coke in a single electrode for gravimetric normalization. For SSA-normalization, values were normalized to the total SSA of the material based on the combined CO₂, N₂ model outlined above.

In addition to capacitance, the equivalent series resistance can be calculated using the constant current cycling data. The equivalent series resistance is the overall cell resistance, including electrical resistance of the current collectors and electrodes, contact resistance between the electrodes and current collectors and the electrodes and separator, and the electrolyte resistance. The equivalent series resistance, in ohms, is calculated by the relationship between voltage drop that occurs when changing from charging to discharging (ΔV) and the charging/discharging current (I), using Eq. 2. The equivalent series resistance affects the rate performance of an EDLC cell since it contributes to the rate at which electrons can travel through the electrodes, and the rate at which ions can diffuse to the carbon surface.

$$ESR = \frac{I}{2\Delta V} \quad (2)$$

3 Results and discussion

3.1 Physical and chemical properties of porous carbon samples

The following section will present the physical and chemical characteristics of the two carbon samples used in this analysis. The similarities and differences in physicochemical properties will be beneficial to identify the causes for variations in EDLC performance.

3.1.1 Porous carbon structure

3.1.1.1 Gas adsorption and pore size distribution analysis The isotherms for both sample types using carbon dioxide or nitrogen gas are presented in Fig. A1 in the electronic supplementary material. The carbon dioxide gas isotherms show similar adsorbed volumes, with the AFC sample having a slightly greater volume adsorbed. The nitrogen isotherms show combined Type I and Type II adsorption isotherms, indicating a mixed microporous and mesoporous structure [54, 55]. The ADC isotherm shows a slightly greater nitrogen gas adsorption, indicating that the surface area of the ADC sample is slightly greater than that of the AFC sample.

The SSA of the ADC and AFC samples are displayed in Fig. 1a with nearly identical values of 2095 and 1960 m² g⁻¹, respectively. The micropore fraction, based on SSA is also displayed, in Fig. 1a. The AFC material has a slightly larger micropore fraction at 0.7, compared to that of the ADC material, which has a micropore fraction of 0.6. The specific pore volume of the porous carbon materials is displayed in Fig. 1b. The ADC sample has a larger specific pore volume of 1.26 cm³ g⁻¹, while the AFC has a specific pore volume of 0.99 cm³ g⁻¹. Based on the microporosity, it is reasonable that the ADC sample would have a larger specific pore volume, since micropores have a lower surface to volume ratio. As such, samples with higher microporosity would be expected to have lower pore volumes, as is observed in the two activated petroleum coke samples.

The pore size distribution of the ADC and AFC samples is displayed in Fig. 1c. The pore size distributions of the two materials again are nearly identical. In the sub-nanometer pore diameter range, the two materials have nearly identical pore size distributions. In the pore size range between 1 and 2 nm, the materials have similar pore sizes; however, the AFC material has a greater volume associated with pores of 1–2 nm in diameter. In contrast, for pores between 2 and 6 nm, the ADC sample has a slightly greater volume associated with these pores; however, again, the pores are of similar diameters.

3.1.1.2 Mercury intrusion porosimetry The cumulative intrusion volume of the ADC and AFC samples calculated using mercury intrusion porosimetry analysis are presented in Fig. 2. The ADC sample has the majority of its pore volume as a result of larger pores between 100,000 and 10,000 nm, with a small portion as a result of pores between 5000 and 10 nm. Similarly, the AFC sample has a portion of its pore volume associated with larger pores between 100,000 and 10,000 nm. However, unlike the ADC sample, the AFC sample also has porosity associated with pores between 1000 and 10 nm.

Fig. 1 **a** Specific surface area (SSA), **b** specific pore volume, and **c** pore size distribution of the activated petroleum coke samples. The values were calculated using density functional theory analysis of carbon dioxide and nitrogen isotherms

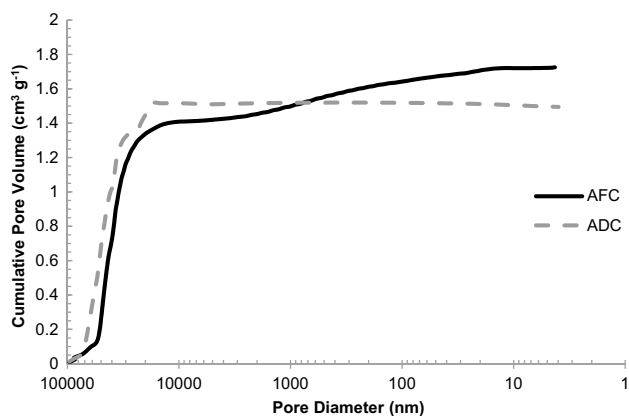
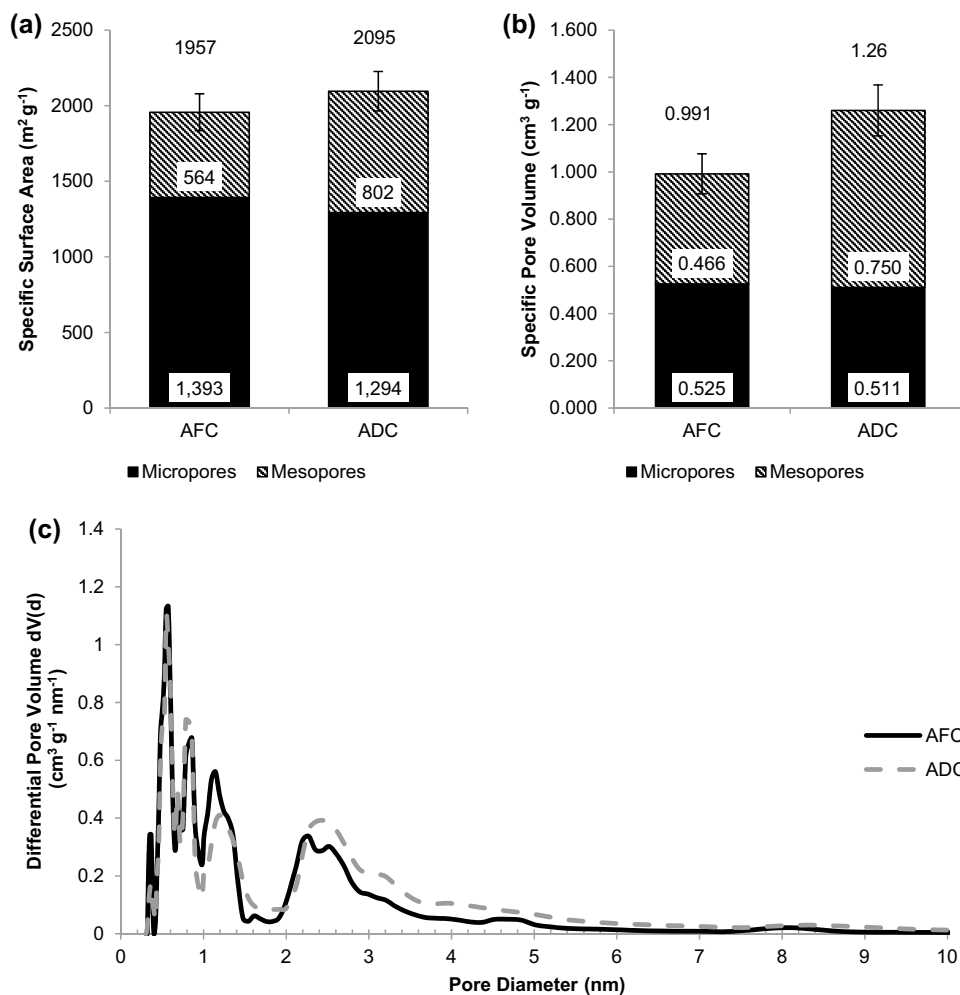


Fig. 2 Mercury intrusion porosimetry analysis of AFC and ADC samples, with cumulative intrusion pore volume compared to pore diameter

The cumulative intrusion volume in Fig. 2 shows that both the ADC and AFC samples have an intrusion volume of 1.3 and 1.4 cm³ g⁻¹ at an approximate pore diameter of

10,000 nm. This result points to the possibility that this porosity may be associated with inter-particle void spacing. However, distinct differences are observed for pores smaller than 10,000 nm. In the ADC sample, there is a jump in pore volume to 1.5 cm³ g⁻¹ at pore diameters of 5000 nm. For pores below 1000 nm in diameter, there appears to be almost no intrusion of mercury. As such, there is very little accessible porosity in the 10–1000 nm range. In the AFC sample, a smooth increase in pore volume is observed between 1000 nm and approximately 10 nm, with an increase in pore volume to 1.7 cm³ g⁻¹. This indicates that there are pores present in the AFC sample with diameters between 10 and 1000 nm in diameter, which contribute to the overall sample pore volume.

By comparing the intrusion profiles, it is clear that mercury smoothly entered the porous structure of the AFC sample, but did not readily penetrate the porous structure of the ADC sample. This smooth intrusion in the AFC sample will potentially translate to improved rate performance in EDLC devices.

3.1.1.3 Carbon density measurements There are two density measurements for porous materials, the skeletal density and the bulk density. The skeletal density of a material measures the density of the pore walls within the structure. In contrast, the bulk density is a measurement of both the skeleton and the void space. Using the relationship between bulk and skeletal density, the void fraction of the powder may be determined as shown in Table 2. It is observed that the skeletal and bulk density of both materials is similar, and that the void fraction of the particles is similar. The void fraction is a combination of the packing density of the particles, as well as the porous structure within the particles.

3.1.2 Electron microscopy imaging

In order to have a visual representation of the differences in macroscopic structure between the AFC and ADC samples, SEM imaging was performed. The two samples are compared at various levels of magnification in Fig. 3.

As can be seen in the scanning electron micrographs, both activated petroleum coke samples have large fractures within the structure. In the lowest magnification images, in Fig. 3a, b (1500× magnification), the macroscopic structure of the ADC is observed to be different from the AFC. The AFC material is composed of many concentric layers of carbon. According to the lower left corner of the image in Fig. 3b, the surface of the layers is composed of highly fractured carbon. By comparing the ADC and AFC surfaces, both appear to be highly fractured. However, the AFC has a considerably higher density of fractures. These macrostructures are consistent with the coking processes used. The ADC material retains its random macrostructure, due to the batch coking process. Similarly, the AFC material retains the layering structure associated with the continuous coking process. However, through chemical activation, the coke particles have fractured, allowing for the electrolyte to access and wet the internal structures.

Further magnification of the surface demonstrates additional differences between the AFC and ADC samples. As seen in the 10,000× magnification image, Fig. 3c, the ADC sample has a very rough surface. In contrast, at the same magnification, in Fig. 3d, the AFC sample appears to have a smoother surface, composed of many layers. Again, the density of fractures is much greater in the AFC sample.

Table 2 Bulk and skeletal density measurements of AFC and ADC samples

	AFC	ADC
Bulk density (g cm ⁻³)	0.35	0.35
Skeletal density (g cm ⁻³)	2.34	2.37
Void fraction	0.85	0.85

The SEM images of both the ADC and AFC samples, obtained at 50,000× magnification, are depicted in Fig. 3e, f, respectively. These micrographs clearly show that the ADC sample has a high surface roughness, with many textures compared to the AFC sample.

These differences in the macrostructure and meso-structure of the ADC and AFC samples are consistent with the mercury intrusion porosimetry results. These images show that the AFC sample has a much higher density of fractures and pores in the larger pore size range, as well as several macroscale channels that allow for ions to diffusion to and from the surface. This is consistent with the smooth intrusion of mercury in the mercury intrusion porosimetry data for pores between 10–1000 nm. Therefore, based on the mercury intrusion porosimetry data and the scanning electron micrographs, the ions in the EDLC electrolyte will likely have improved diffusion in the highly fractured and meso- and macroporous AFC sample compared to the less meso- and macroporous ADC sample.

3.1.3 Chemical composition

3.1.3.1 Elemental chemical analysis Elemental analysis of the carbon materials demonstrated is displayed in Table 3. The carbon content of the ADC and AFC is greater than 90 wt%. The sulfur content of the AFC and ADC materials is approximately 1 wt%, the nitrogen and hydrogen content is <1 wt%, and the oxygen content is 2.5–4 wt%. The chemical composition of AFC and ADC is very similar. This consistency between the chemical compositions of the two samples indicates that there would be limited variations in performance associated with electrolyte wettability and rapid faradaic charge transfer reactions. Therefore, this makes these two samples ideal to compare variations in EDLCs performance associated with structural differences.

3.1.3.2 X-ray photoelectron spectroscopy In order to characterize the oxygen functional groups, X-ray photoelectron spectroscopy analysis was performed. The X-ray photoelectron spectroscopy results are presented in Table 4, with the raw data presented in Fig. A2 of the electronic supplementary material. The pH of both the concentrated and dilute electrolyte is greater than 13.5. In previous studies, it has been shown that in highly alkaline electrolytes, that phenol and carboxyl groups are electrochemically active and undergo charge transfer reactions, which can contribute to the capacitance [57–59]. The atomic percentage of electrochemically active oxygen functional groups on the surface of the ADC and AFC materials was quantified using X-ray photoelectron spectroscopy. This information can be used to determine if variations in the performance of the ADC and AFC electrodes can be attributed to variations in surface oxygen functional groups.

Fig. 3 Scanning electron micrographs of ADC (a, c, e) and AFC (b, d, f) at various magnifications using an accelerating voltage of 500 V

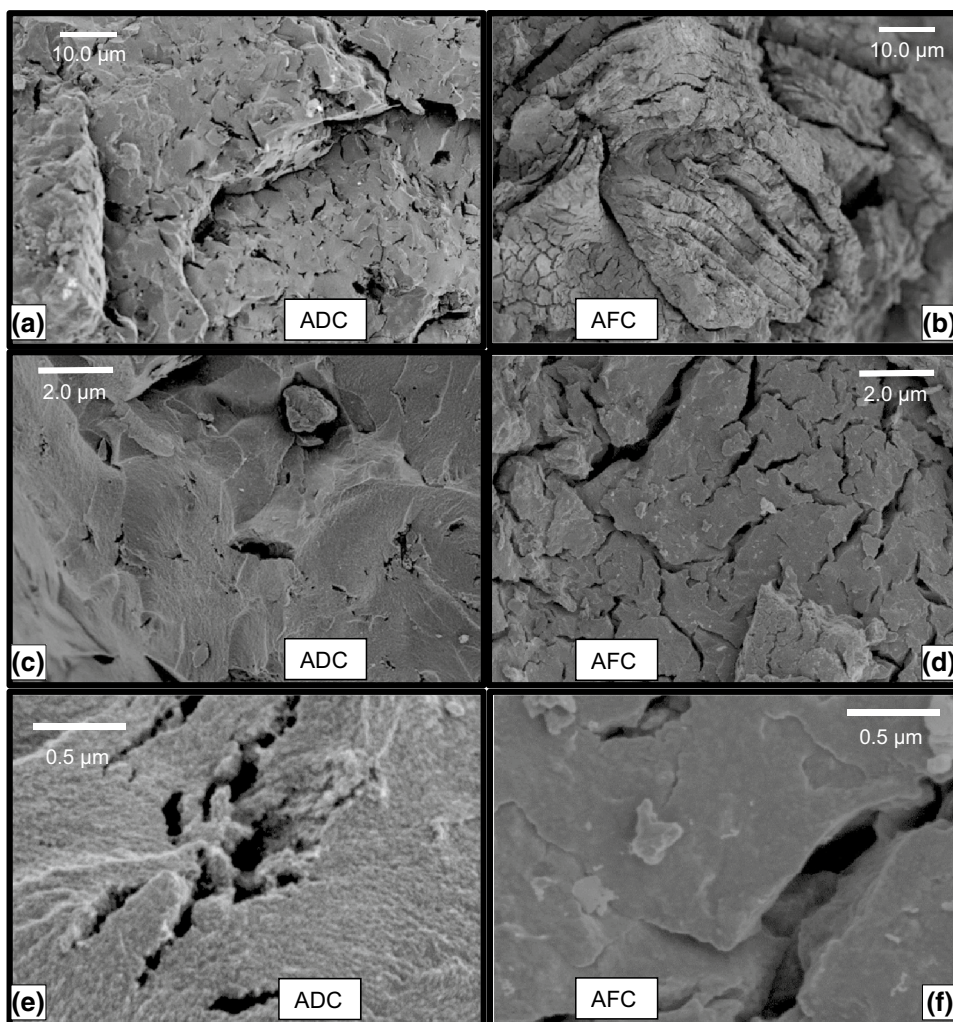


Table 3 Elemental chemical analysis of AFC and ADC

	C	H	N	S	O
AFC	91.1 ± 1.5	0.5 ± 0.1	0.3 ± 0.02	0.8 ± 0.10	2.7 ± 0.4
ADC	94.9 ± 2.2	0.6 ± 0.1	0.4 ± 0.13	1.2 ± 0.12	3.8 ± 0.5

The X-ray photoelectron spectroscopy results show that the atomic percentage of phenol groups, based on total sample, is 0.8 at.% for both the ADC and AFC carbon materials. Similarly, the atomic percentage of carboxyl groups, based on total sample, for the AFC and ADC

Table 4 X-ray photoelectron spectroscopy results for oxygen functional groups of the activated petroleum coke samples, given in atomic percentage based on total oxygen and total sample

Functional group	Binding energy (eV)	Activated fluid coke (AFC)		Activated delayed coke (ADC)	
		Percentage of total oxygen (at.%)	Percentage of total sample (at.%)	Percentage of total oxygen (at.%)	Percentage of total sample (at.%)
Quinone	530.5	14.8	1.2	15.1	0.8
Carbonyl	533.1	47.9	4	35.8	1.9
Carboxyl	531.8	20.6	1.7	24.7	1.3
Phenol	534.6	9.2	0.8	14.9	0.8
Chemisorbed oxygen	536.9	7.4	0.6	9.5	0.5

materials is 1.7 and 1.3 at.%, respectively. Therefore, the total amount of electrochemically active oxygen functional groups is similar for both the AFC and ADC materials. As such, the X-ray photoelectron spectroscopy results indicate that the effect of oxygen functional groups is expected to be similar for both activated petroleum coke materials, and would not affect the relationship between carbon meso- and macrostructure and capacitance as a functional of charging rate.

3.1.4 Summary of physicochemical similarities and difference

Table 5 provides a summary of the physical and chemical characteristics of the two activated coke samples. While most of the physical and chemical properties are similar, the two main differences are the specific pore volume and the mesoscale and macroscale structure, as analyzed by SEM imaging. Therefore, these two samples provide a unique comparison on the relationship between mesopore and macropore structure and EDLC device performance, focusing on the charging rate.

3.2 Electrochemical performance

This study investigated the relationship between macroscale and mesoscale structure and pores, and the rate performance of activated petroleum coke materials. In order to investigate the rate performance, the capacitance of both the ADC and AFC was measured in a 2-electrode test cell, at a current density between 25 and 7500 mA g⁻¹, and at a sweep rate between 1 and 100 mV s⁻¹, for a potential window of 0.8 V.

Table 5 Summary of physical and chemical characteristics of the AFC and the ADC samples

Parameter	AFC	ADC
Specific surface area	1960 m ² g ⁻¹	2095 m ² g ⁻¹
Specific pore volume	0.99 cm ³ g ⁻¹	1.26 cm ³ g ⁻¹
Microporosity (SSA based)	0.71	0.62
Visible mesoscale and macroscale structure (SEM)	Concentric layering, highly fractured, smooth surface	Moderate fracturing, rough surface
Mercury porosimetry structure	Smooth intrusion, porosity between 10 and 1000 nm	Lack of porosity between 10 and 1000 nm
Tap density	0.35 g cm ⁻³	0.35 g cm ⁻³
Skeletal density	2.34 g cm ⁻³	2.37 g cm ⁻³
Void fraction	0.851	0.852
Chemical analysis	Similar	Similar

3.2.1 Performance in electrochemical double-layer capacitor device

The maximum measured capacitance, measured at a scan rate of 1 mV s⁻¹, of the ADC and AFC samples are similar, as presented in Table 6. Additionally, the cyclic voltammograms presented in Fig. A3 in the electronic supplementary material show similar behavior of the ADC and AFC samples at slow charging rates. In the concentrated 4 M KOH electrolyte, a gravimetric capacitance of 302 F g⁻¹ was estimated for the ADC electrodes, compared to 258 F g⁻¹ for the AFC electrodes. This result is unexpected given the similar SSA values. However, when the capacitance is normalized to total SSA, the AFC and ADC materials have similar values, at 13.1 and 14.4 μF cm⁻², respectively, which is expected based on the similar pore size distribution of the materials. The variation in gravimetric capacitance can, therefore, be explained by the slightly higher SSA of the ADC material.

In the dilute 0.4 M KOH electrolyte, the gravimetric capacitances of the ADC and AFC materials are similar, 225 and 217 F g⁻¹, respectively. In the dilute solution, the capacitance of the ADC material is only 3% greater than that of the AFC material, compared to a 16% difference in the concentrated electrolyte. This result suggests that the measured SSA of the ADC material may not be as readily accessible as the AFC material. As described above, the AFC material has distinct layered structures, which may promote ion diffusion and penetration into the center of the carbon particles. To further investigate the relationship between the macroscopic structure and ion diffusion, the rate performance of the two materials was analyzed.

3.2.2 Rate performance in variable electrolyte concentrations

As discussed in the introduction, the rate performance is the relationship between measured capacitance and the

Table 6 Capacitance of ADC and AFC electrodes in 4 M KOH electrolyte and 0.4 M KOH electrolyte, measured using cyclic voltammetry at a scan rate of 1 mV s⁻¹ and potential window of 0.8 V. The gravimetric capacitance is normalized to the mass of activated coke in a single electrode, and the SSA-normalized capacitance is normalized to the SSA of the activated coke in a single electrode

Electrode material	Specific surface area (m ² g ⁻¹)	4 M KOH electrolyte		0.4 M KOH electrolyte	
		Gravimetric capacitance (F g ⁻¹)	SSA-normalized capacitance (μF cm ⁻²)	Gravimetric capacitance (F g ⁻¹)	SSA-normalized capacitance (μF cm ⁻²)
ADC	2095	302	14.4	225	10.8
AFC	1960	258	13.1	217	11.1

charging/discharging rate. The rate performance can also be described as capacitance retention and is presented as a percentage of the maximum measurable capacitance, which is achieved at the lowest charging rate. The rate performance of different carbon materials can be compared based on the slope of the capacitance retention against current density or sweep rate, as shown in Fig. 4. The rate performance of the ADC and AFC materials are similar in the highly concentrated 4 M KOH electrolyte as shown in Fig. 4. For the constant current cycling, in Fig. 4a, the ADC material has a slightly better rate performance than the AFC material. At the highest current density, 7500 mA g⁻¹, the ADC material retains 82% of the maximum measured capacitance at 25 mA g⁻¹. At the same charging current of 7500 mA g⁻¹, the AFC material retains 69% of the maximum measured capacitance at 25 mA g⁻¹. However, the rate performance and capacitance retention of these materials is fairly similar. In the cyclic voltammetry analysis, the rate performance of both the AFC and ADC materials is nearly identical, as seen in Fig. 4b. At a sweep rate of 100 mV s⁻¹, the retained capacitance for both materials is greater than 45% compared to charging at 1 mV s⁻¹.

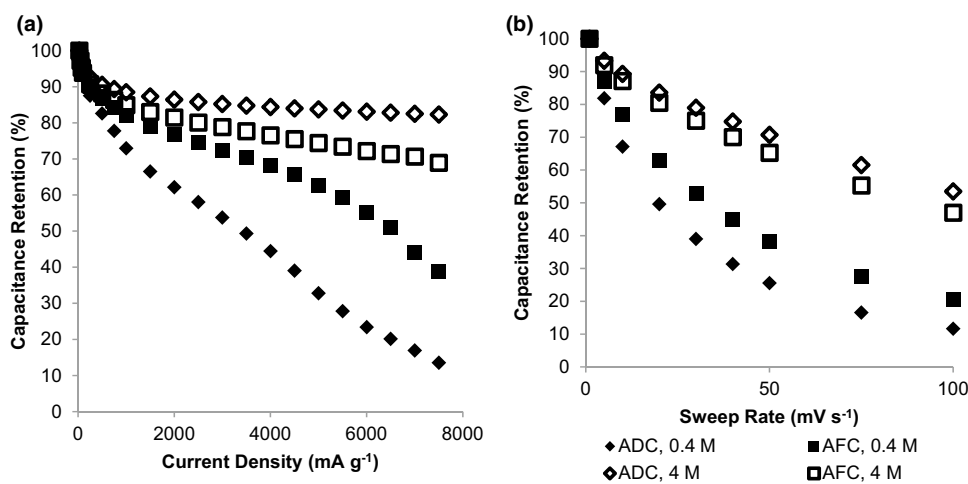
While the 4 M KOH electrolyte demonstrates an ion rich electrolyte, which is not likely to be depleted of ions during charging, the rate performance can be greatly affected by depletion of electrolyte ions. In order to investigate the performance in an ion depleted scenario, the concentration of the electrolyte was decreased ten-fold to a 0.4 M KOH solution. The results of the dilute electrolyte solution are displayed in Fig. 4, for comparison to the concentrated elec-

material has retained a significantly larger percentage of its maximum capacitance at higher charging rates. In the AFC sample, the measured capacitance at 7500 mA g⁻¹ is 39% of that measured at 25 mA g⁻¹. Compared to the measured capacitance at 25 mA g⁻¹, the ADC sample has retained a much poorer capacitance of 14% at 7500 mA g⁻¹. Similarly, in cyclic voltammetry operation, the measured capacitance at 100 mV s⁻¹ is 21% and 12% of that measured at 1 mV s⁻¹, for the AFC and ADC samples, respectively. The rate performance normalized to mass of active material in a single electrode for both constant current and cyclic voltammetry testing is presented in the electronic supplementary material.

As expected, the measured capacitance at higher charging rates is lower compared to the maximum measured capacitance at 25 mA g⁻¹. This is observed in both the AFC and ADC materials for both cyclic voltammetry and constant current analyses, as shown in supplementary material. Since there are ten times fewer ions present in the electrolyte solution, the solution is more likely to be depleted of ions during charging. In contrast, the highly concentrated 4 M KOH electrolyte will have ample ions, thus limiting or eliminating the effects of electrolyte ion depletion and diffusion.

The equivalent series resistance of the EDLC test devices is a measure of the total cell resistance, including the electrodes, the dielectric separator, and the electrolyte, as discussed in the “Experimental” section. In the concentrated 4 M KOH cell, the equivalent series resistance of both the AFC and ADC test devices was 0.5 Ω. The low overall cell resistance indicates that the resistance of both the AFC and ADC electrode materials is not significant. Therefore, the

Fig. 4 Rate performance of activated petroleum coke electrodes, for a potential window of 0.8 V, in 4 M KOH and 0.4 M KOH aqueous electrolyte **a** for current densities between 25 and 7500 mA g⁻¹, standardized capacitance is the ratio of the measured capacitance at a given current density compared to the measured at 25 mA g⁻¹, and **b** for sweep rates between 1 and 100 mV s⁻¹, standardized capacitance is the ratio of the measured capacitance at a given sweep rate compared to the measured at 1 mV s⁻¹



trolyte. The use of a low concentration electrolyte, will allow for the effects of ion diffusion in the AFC and ADC electrodes to be more easily observed.

In the 0.4 M KOH electrolyte solution, in both cyclic voltammetry and constant current testing methods, the AFC

low resistance of the AFC and ADC materials will not affect the rate performance of the EDLC test devices in either the concentrated or dilute KOH electrolyte.

3.3 Discussion and interpretation of results

In comparing the two activated petroleum coke samples, there are some distinct structural features that are similar and some distinct structural features that are different. By comparing the similarities and differences in the activated coke samples with the electrochemical performance of the samples, it is possible to identify key structural features that impact EDLC device performance. Since the chemical composition and atomic percentage of electrochemically active oxygen functional groups of the two samples are similar, it is unlikely that variations in performance are associated with electrolyte wettability or faradaic charge transfer reactions. The SSAs of both samples are similar for pores below 10 nm in diameter, as are the pore size distributions in this range. Both the ADC and AFC samples have similar SSA-normalized capacitance values at the slowest charging rates. Given that the pore size distribution and SSA for pores below 10 nm is similar, it is likely that these pore sizes affect the maximum achievable SSA-normalized capacitance values.

There are two key distinct differences between the two activated coke samples, the specific pore volume, and the mesoscale and macroscale structural cracking. The specific pore volume of the ADC samples is $1.26 \text{ cm}^3 \text{ g}^{-1}$, while the specific pore volume of the AFC sample is $0.99 \text{ cm}^3 \text{ g}^{-1}$. A larger specific pore volume would allow a larger volume of electrolyte to reside in the pores of the carbon, and lower the distance that the ion must diffuse to adsorb on the surface during charging. Since the ADC sample has a larger specific pore volume than the AFC sample, the rate performance of the ADC material might be expected to be better than that of the AFC material. However, the AFC material has similar rate performance in the concentrated electrolyte and significantly better rate performance in the dilute electrolyte. Therefore, it is unlikely that the variations in specific pore volume for pores less than 10 nm in diameter are affecting the rate performance of the device.

The variations in mesoscale and macroscale structure observed using SEM and the mercury intrusion porosimetry analysis demonstrate a significant difference in material structure. As discussed above, the ADC sample has many small fractures; however, the AFC sample has concentric layers, with gaps in between, which would allow the electrolyte to more readily migrate into the porous structure. The visible differences in pore structure were confirmed with mercury intrusion porosimetry analysis. Based on the mercury intrusion porosimetry analysis, the AFC sample had a smooth intrusion of mercury into pores from 1000 to 10 nm. In contrast, the ADC sample had almost no intrusion over this range, indicating almost a complete lack of porosity associated with this pore range. Based on the rate performance results, these moderately sized ion diffusion

channels appear to play an important role for ion diffusion and transport.

Therefore, combining the gas adsorption, mercury intrusion porosimetry, SEM, and EDLC rate performance results, several observations may be made. It is observed that both the ADC and AFC have similar SSA-normalized capacitance values in the 4 M KOH and 0.4 M KOH electrolyte at the slowest charging rates. As such, it can be concluded that the intrinsic or maximum capacitance of a material is primarily affected by the small mesopores and micropores.

The large mesopores and macropores are critical to allow for rapid ion diffusion into the porous structure, and improve the rate performance of a material. The presence of the well-connected, concentric layering of the AFC sample results in a significant improvement in rate performance for the ion depleted electrolyte. Therefore, the results suggest that pores between 10 and 1000 nm are critical for high power applications.

4 Conclusions

Ion diffusion into and out of porous carbon EDLC electrodes is critical to maximize the rate performance and power delivery of a material. In this study, AFC and ADC are compared in order to identify key structural features that enhance EDLC performance. The AFC and ADC samples have similar pore size distributions and total SSA associated with pores of diameters < 10 nm in diameter. The main structural differences between the AFC and ADC samples is the large mesopores and macropore structure as observed using mercury intrusion porosimetry and SEM. By comparing the electrochemical performance of these devices in EDLCs, the relationship between different structural features and EDLC performance has been investigated.

There are two main conclusions that can be drawn from this analysis.

1. The micropores and small mesopores primarily affect the SSA-normalized capacitance of a material. Both the ADC and AFC samples have similar structures in this range and similar SSA-normalized capacitance values.
2. A well-connected meso-structure and macrostructure, with rapid diffusion is critical for improved rate performance, especially in ion depleted electrolytes. This was achieved by the pores in the AFC sample with diameters between 10 and 1000 nm.

Therefore, based on these results, depending on the application, it is critical to achieve a good balance in pore size distribution. A large surface area associated with sub-nanometer micropores and small mesopores is required in order to maximize intrinsic capacitance and energy density.

However, it is also critical to ensure that the meso-structure and macrostructure are interconnected allowing for rapid electrolyte diffusion. This will ensure that ions can rapidly move to and from the electrode surface during charging.

Acknowledgements The authors would like to acknowledge the Natural Science and Engineering Research Council (NSERC), the Consortium on Sustainable Materials (COSM-Japan) and the Chinese–NSF for funding for this project. As well, the authors would like to thank the Canadian Oil Sands industry for supply of raw petroleum coke. The authors would also like to thank Professor Tim Newson and Dr. Nael Yasri from Western University for their help with the Mercury Intrusion Porosimetry analysis. The authors would also like to thank Dr. Rana Sodhi from the University of Toronto for his help with the X-ray photoelectron spectroscopy analysis.

References

- Conway BE (1999) *Electrochemical supercapacitors, scientific fundamentals and technological applications*. Kluwer Academic, Ottawa
- Burke A (2000) Ultracapacitors: why, how, and where is the technology. *J Power Sources* 91:37–50. doi:10.1016/S0378-7753(00)00485-7
- Kotz R, Carlen M (2000) Principles and applications of electrochemical capacitors. *Electrochim Acta* 45:2483–2498. doi:10.1016/S0013-4686(00)00354-6
- Pandolfo AG, Hollenkamp AF (2006) Carbon properties and their role in supercapacitors. *J Power Sources* 157:11–27. doi:10.1016/j.jpowsour.2006.02.065
- Frackowiak E, Beguin F (2001) Carbon materials for the electrochemical storage of energy in capacitors. *Carbon* 39:937–950. doi:10.1016/S0008-6223(00)00183-4
- Ghosh A, Lee YH (2012) Carbon-based electrochemical capacitors. *Chem Sus Chem* 5:480–499. doi:10.1002/cssc.201100645
- Gu WT, Yushin G (2014) Review of nanostructured carbon materials for electrochemical capacitor applications: advantages and limitations of activated carbon, carbide-derived carbon, zeolite-templated carbon, carbon aerogels, carbon nanotubes, onion-like carbon, and graphene. *WIREs-Energy Environ* 3:424–473. doi:10.1002/wene.102
- Inagaki M, Konno H, Tanaike O (2010) Carbon materials for electrochemical capacitors. *J Power Sources* 195:7880–7903. doi:10.1016/j.jpowsour.2010.06.036
- Zhai YP, Dou YQ, Zhao DY, Fulvio PF, Mayes RT, Dai S (2011) Carbon materials for chemical capacitive energy storage. *Adv Mater* 23:4828–4850. doi:10.1002/adma.201100984
- Zhang LL, Zhao XS (2009) Carbon-based materials as supercapacitor electrodes. *Chem Soc Rev* 38:2520–2531. doi:10.1039/b813846j
- Davies A, Yu A (2011) Material advancements in supercapacitors: from activated carbon to carbon nanotube and graphene. *Can J Chem Eng* 89:1342–1357. doi:10.1002/cjce.20586
- Simon P, Gogotsi Y (2008) Materials for electrochemical capacitors. *Nat Mater* 7:845–854. doi:10.1038/nmat2297
- Simon P, Gogotsi Y (2013) Capacitive energy storage in nanostructured carbon-electrolyte systems. *Acc Chem Res* 46:1094–1103. doi:10.1021/ar200306b
- Frackowiak E, Abbas Q, Beguin F (2013) Carbon/carbon supercapacitors. *J Energ Chem* 22:226–240. doi:10.1016/S2095-4956(13)60028-5
- Beguin F, Presser V, Balducci A, Frackowiak E (2014) Carbons and electrolytes for advanced supercapacitors. *Adv Mater* 26:2219–2251. doi:10.1002/adma.201304137
- Simon P, Gogotsi Y (2010) Charge storage mechanism in nanoporous carbons and its consequence for electrical double layer capacitors. *Philos Trans R Soc A* 368:3457–3467. doi:10.1098/rsta.2010.0109
- Chmiola J, Yushin G, Gogotsi Y, Portet C, Simon P, Taberna PL (2006) Anomalous increase in carbon capacitance at pore sizes less than 1 nanometer. *Science* 313:1760–1763. doi:10.1126/science.1132195
- Chmiola J, Largeot C, Taberna PL, Simon P, Gogotsi Y (2008) Desolvation of ions in subnanometer pores and its effect on capacitance and double-layer theory. *Angew Chem* 120:3440–3443. doi:10.1002/ange.200704894
- Alonso A, Ruiz V, Blanco C, Santamaria R, Granda M, Menendez R, de Jager SGE (2006) Activated carbon produced from sasol-lurgi gasifier pitch and its application as electrodes in supercapacitors. *Carbon* 44:441–446. doi:10.1016/j.carbon.2005.09.008
- Kierzek K, Frackowiak E, Lota G, Gryglewicz G, Machnikowski J (2004) Electrochemical capacitors based on highly porous carbons prepared by KOH activation. *Electrochim Acta* 49:515–523. doi:10.1016/j.electacta.2003.08.026
- Centeno TA, Stoeckli F (2006) On the specific double-layer capacitance of activated carbons, in relation to their structural and chemical properties. *J Power Sources* 154:314–320. doi:10.1016/j.jpowsour.2005.04.007
- Centeno TA, Fernandez JA, Stoeckli F (2008) Correlation between heats of immersion and limiting capacitances in porous carbons. *Carbon* 46:1025–1030. doi:10.1016/j.carbon.2008.03.005
- Centeno TA, Sereda O, Stoeckli F (2011) Capacitance in carbon pores of 0.7 to 15 nm: a regular pattern. *Phys Chem Chem Phys* 13:12403–12406. doi:10.1039/c1cp20748b
- Lazzari M, Soavi F, Mastragostino M (2010) Mesoporous carbon design for ionic liquid-based, double-layer supercapacitors. *Fuel Cells* 10:840–847. doi:10.1002/fuce.200900198
- Jäckel N, Rodner M, Schreiber A, Jeongwook J, Zeiger M, Aslan M, Weingarth D, Presser V (2016) Anomalous or regular capacitance? the influence of pore size dispersity on double-layer formation. *J Power Sources* 326:660–671. doi:10.1016/j.jpowsour.2016.03.015
- Chmiola J, Yushin G, Dash R, Gogotsi Y (2006) Effect of pore size and surface area of carbide derived carbons on specific capacitance. *J Power Sources* 158:765–772. doi:10.1016/j.jpowsour.2005.09.008
- Kondrat S, Kornyshev A (2011) Superionic state in double-layer capacitors with nanoporous electrodes. *J Phys* 23:022201. doi:10.1088/0953-8984/23/2/022201
- Kondrat S, Perez CR, Presser V, Gogotsi Y, Kornyshev AA (2012) Effect of pore size and its dispersity on the energy storage in nanoporous supercapacitors. *Energy Environ Sci* 5:6474–6479. doi:10.1039/c2ee03092f
- Merlet C, Rotenberg B, Madden PA, Taberna PL, Simon P, Gogotsi Y, Salanne M (2012) On the molecular origin of supercapacitance in nanoporous carbon electrodes. *Nat Mater* 11:306–310. doi:10.1038/nmat3260
- Levi MD, Sigalov S, Salitra G, Aurbach D, Maier J (2011) The effect of specific adsorption of cations and their size on the charge-compensation mechanism in carbon micropores: the role of anion desorption. *Chem Phys Phys Chem* 12:854–862. doi:10.1002/cphc.201000653
- Levi MD, Sigalov S, Salitra G, Elazari R, Aurbach D (2011) Assessing the solvation numbers of electrolytic ions confined in carbon nanopores under dynamic charging conditions. *J Phys Chem Lett* 2:120–124. doi:10.1021/jz1016922

32. Daffos B, Taberna PL, Gogotsi Y, Simon P (2010) Recent advances in understanding the capacitive storage in microporous carbons. *Fuel Cells* 10:819–824. doi:10.1002/fuce.200900192
33. Chathoth SM, Mamontov E, Kolesnikov AI, Gogotsi Y, Wesolowski DJ (2011) Quasielastic neutron scattering study of water confined in carbon nanopores. *EPL* 95:56001. doi:10.1209/0295-5075/95/56001
34. Tsai WY, Taberna PL, Simon P (2014) Electrochemical quartz crystal microbalance (EQCM) study of ion dynamics in nanoporous carbons. *J Am Chem Soc* 136:8722–8728. doi:10.1021/ja503449w
35. Merlet C, Pean C, Rotenberg B, Madden PA, Daffos B, Taberna PL, Simon P, Salanne M (2013) Highly confined ions store charge more efficiently in supercapacitors. *Nat Commun* 4:2701. doi:10.1038/ncomms3701
36. Garcia-Gomez A, Barranco V, Moreno-Fernandez G, Ibanez J, Centeno TA, Rojo JM (2014) Correlation between capacitance and porosity in microporous carbon monoliths. *J Phys Chem C* 118:5134–5141. doi:10.1021/jp411076a
37. Ohkubo T, Konishi T, Hattori Y, Kanoh H, Fujikawa T, Kaneko K (2002) Restricted hydration structures of Rb and Br ions confined in slit-shaped carbon nanospace. *J Am Chem Soc* 124:11860–11861. doi:10.1021/ja027144t
38. Zuliani JE, Tong S, Kirk DW, Jia CQ (2015) Isolating the effect of pore size distribution on electrochemical double-layer capacitance using activated fluid coke. *J Power Sources* 300:190–198. doi:10.1016/j.jpowsour.2015.09.030
39. Wang DW, Li F, Liu M, Lu GQ, Cheng HM (2009) 3D aperiodic hierarchical porous graphitic carbon material for high-rate electrochemical capacitive energy storage. *Angew Chem Int Ed Engl* 47:373–376. doi:10.1002/anie.200702721
40. Korenblit Y, Rose M, Kockrick E, Borchardt L, Kvit A, Kaskel S, Yushin G (2010) High-rate electrochemical capacitors based on ordered mesoporous silicon carbide-derived carbon. *ACS Nano* 4:1337–1344. doi:10.1021/nn901825y
41. Li Y, Fu ZY, Su BL (2012) Hierarchically structured porous materials for energy conversion and storage. *Adv Funct Mater* 22:4634–4667. doi:10.1002/adfm.201200591
42. Kim M, Oh I, Kim J (2015) Supercapacitive behavior depending on the mesopore size of three-dimensional micro-, meso- and macroporous silicon carbide for supercapacitors. *Phys Chem Chem Phys* 17:4424–4433. doi:10.1039/c4cp05357e
43. Qu D, Shi H (1998) Studies of activated carbons used in double-layer capacitors. *J Power Sources* 74:99–107. doi:10.1016/S0378-7753(98)00038-X
44. Yamada Y, Sasaki T, Tatsuda N, Weingarth D, Yano K, Kötze R (2012) A novel model electrode for investigating ion transport inside pores in an electrical double-layer capacitor: monodispersed microporous starburst carbon spheres. *Electrochim Acta* 81:138–148. doi:10.1016/j.electacta.2012.07.064
45. Wu ZS, Sun Y, Tan YZ, Yang SB, Feng XL, Mullen K (2012) Three-dimensional graphene-based macro- and mesoporous frameworks for high-performance electrochemical capacitive energy storage. *J Am Chem Soc* 134:19532–19535. doi:10.1021/ja308676h
46. Furimsky E (2000) Characterization of cokes from fluid/flexicoking of heavy feeds. *Fuel Process Technol* 67:205–230. doi:10.1016/S0378-3820(00)00103-x
47. DiPanfilo R, Egiebor NO (1996) Activated carbon production from synthetic crude coke. *Fuel Process Technol* 46:157–169. doi:10.1016/0378-3820(95)00054-2
48. Zuliani JE, Kirk DW, Jia CQ, Tong S (2014) Activated oil sands fluid coke for electrical double-layer capacitors. *J Power Sources* 271:326–333. doi:10.1016/j.jpowsour.2014.07.171
49. Yuan M, Kim Y, Jia CQ (2012) Feasibility of recycling koh in chemical activation of oil-sands petroleum coke. *Can J Chem Eng* 90:1472–1478. doi:10.1002/cjce.20671
50. Furimsky E (1998) Gasification of oil sand coke: review. *Fuel Process Technol* 56:263–290. doi:10.1016/S0378-3820(98)00048-4
51. Cai JH, Jia CQ (2010) Mercury removal from aqueous solution using coke-derived sulfur-impregnated activated carbons. *Ind Eng Chem Res* 49:2716–2721. doi:10.1021/ie901194r
52. Jagiello J, Ania C, Parra JB, Cook C (2015) Dual gas analysis of microporous carbons using 2D-NLDFT heterogeneous surface model and combined adsorption data of N₂ and CO₂. *Carbon* 91:330–337. doi:10.1016/j.carbon.2015.05.004
53. Caguait JN, Kirk DW, Jia CQ (2014) Uncertainties in characterization of nanoporous carbons using density functional theory-based gas physisorption. *Carbon* 72:47–56. doi:10.1016/j.carbon.2014.01.036
54. Brunauer S, Deming LS, Deming WE, Teller E (1940) On a theory of the van der Waals adsorption of gases. *J Am Chem Soc* 62:1723–1732. doi:10.1021/ja01864a025
55. Sing KSW, Everett DH, Haul RAW, Moscou L, Pierotti RA, Rouquerol J, Siemieniowska T (1985) Reporting physisorption data for gas/solid systems, with special references to the determination of surface area and porosity. *Pure Appl Chem* 57:603–619
56. Giesche H (2006) Mercury porosimetry: a general (practical) overview. *Part Part Sts Char* 23:9–19. doi:10.1002/ppsc.200601009
57. Chen CM, Zhang Q, Zhao XC, Zhang B, Kong QQ, Yang MG, Yang QH, Wang MZ, Yang YG, Schlogl R, Su DS (2012) Hierarchically aminated graphene honeycombs for electrochemical capacitive energy storage. *J Mater Chem* 22:14076–14084. doi:10.1039/C2JM31426F
58. Oh YJ, Yoo JJ, Kim YI, Yoon JK, Yoon HN, Kim J-H, Park SB (2014) Oxygen functional groups and electrochemical capacitive behavior of incompletely reduced graphene oxides as a thin-film electrode of supercapacitor. *Electrochim Acta* 116:118–128. doi:10.1016/j.electacta.2013.11.040
59. Fang Y, Luo B, Jia Y, Li X, Wang B, Song Q, Kang F, Zhi L (2012) Renewing functionalized graphene as electrodes for high-performance supercapacitors. *Adv Mater* 24:6348–6355. doi:10.1002/adma.201202774